

Multi-Mode Front Lens for Momentum Microscopy: Part II Experiments

O. Tkach^{1,2}, S. Fragkos³, Q. Nguyen⁴, S. Chernov⁵, M. Scholz⁵, N. Wind^{5,6}, S. Babenkov¹, O. Fedchenko¹, Y. Lytvynenko¹, D. Zimmer¹, A. Hloskovskii⁵, D. Kutnyakhov⁵, F. Pressacco⁵, J. Dilling^{5,8}, L. Bruckmeier^{5,8}, M. Heber⁵, F. Scholz⁵, J. A. Sobota^{4,9}, J. D. Koralek⁴, N. Sirica¹⁰, M. Kallmayer⁷, M. Hoesch⁵, C. Schlueter⁵, L.V. Odnodvoretz², Y. Mairesse³, K. Rossnagel^{5,8,11}, H.-J. Elmers¹, S. Beaulieu³ and G. Schönhense^{1*}

1 Johannes Gutenberg-Universität, Institut für Physik, D-55099 Mainz, Germany

2 Sumy State University, Rymskogo-Korsakova 2, 40007 Sumy, Ukraine

3 Université de Bordeaux - CNRS - CEA, CELIA, UMR5107, F33405 Talence, France

4 SLAC National Acceleration Laboratory, Menlo Park, CA 94025, USA

5 Deutsches Elektronen-Synchrotron DESY, D-22607 Hamburg, Germany

6 University of Hamburg, Institut für Experimentalphysik, D-22761 Hamburg, Germany

7 Surface Concept GmbH, Mainz, Germany

8 Institut für Experimentelle und Angewandte Physik, Christian-Albrechts-Universität zu Kiel, D-24098 Kiel, Germany

9 Stanford University, Stanford, CA 94305, USA

10 Los Alamos National Laboratory, Santa Fe, NM 87545, USA

11 Ruprecht Haensel Laboratory, Deutsches Elektronen-Synchrotron DESY, D-22607 Hamburg, Germany

* corresponding author: schoenhe@uni-mainz.de

Abstract

We have experimentally demonstrated different operating modes for the front lenses of the momentum microscopes described in Part I. Measurements at energies from vacuum UV at a high-harmonic generation (HHG)-based source to the soft and hard X-ray range at a synchrotron facility validated the results of theoretical ray-tracing calculations. The key element is a ring electrode concentric with the extractor electrode, which can tailor the field in the gap. First, the *gap-lens-assisted extractor mode* reduces the field strength at the sample while mitigating image aberrations. This mode gave good results in all spectral ranges. Secondly, by compensating the field at the sample surface with a negative voltage at the ring electrode we can operate in *zero-field mode*, which is beneficial for operando experiments. Finally, higher negative voltages establish the *repeller mode*, which removes all slow electrons below a certain kinetic energy to eliminate the primary contribution to the space-charge interaction in pump-probe experiments. The switch from *extractor* to *repeller mode* is associated with a reduction in the *k*-field-of-view (10-20% at hard-X-ray energies, increasing to ~50% at low energies). Real-space imaging also benefits from the new lens modes as confirmed by ToF-XPEEM imaging with 650 nm resolution.

1. Introduction

Photoelectron momentum microscopy (MM) offers a complementary approach to angle-resolved photoelectron spectroscopy (ARPES). MM can simultaneously record large phase-space intervals, which is particularly advantageous for low-intensity experiments like hard-X-ray photoemission or when many experimental parameters need to be varied, like in ultrafast femtosecond time-resolved photoelectron spectroscopy (tr-PES). Momentum microscopes use the so-called ‘cathode lenses’, whose key feature induces a high electrostatic field (extractor field) at the sample surface. For photoelectron kinetic energies of up to $\sim 100\text{eV}$, the instrument collects all photoelectrons in the full 2π solid angle interval, where the 2D (k_x, k_y) momentum distribution exhibits a linear lateral k -scale with high k -resolution.

Previous work has developed different approaches to energy recording, including an early attempt using a simple retarding-field energy filter [1], later designs using tandem configurations of two hemispherical analyzers [2-4], followed by single hemispherical analyzers [5-7]. We have achieved unprecedented efficiency with the latest time-of-flight (ToF) energy recording technique that enables simultaneous 3D $(k_x, k_y, E_{\text{kin}})$ data acquisition [8].

The extractor-field approach combined with ToF energy recording offers advantages with remaining limitations, which we will address in this article. In particular, the high electric field can cause field emission or flashovers at the edges of cleaved samples, or microscopic defects like protruding lamellae of layered samples. The unique collection efficiency also acts on ‘unwanted’ background electrons with low kinetic energies. The secondary electrons related to the true photoelectron signal or electrons generated by a strong pump pulse in the visible, infrared or mid-infrared spectral range are also pulled into the microscope column. The slow electrons exert Coulomb repulsion on the photoelectrons that causes space-charge shifts and broadening (more details discussed in Ref. [9]). Meanwhile, the high collecting efficiency and good lateral resolution of the extractor field deteriorate with increasing photoelectron kinetic energy. The equations for the spherical and chromatic aberration reveal that both increase with increasing initial kinetic energy.

Part I of this article [10] presents the theoretical basis to address these issues, such as replacing the homogeneous extractor field by specially-shaped lens fields in the gap between sample and extractor. One or several concentric ring-shaped electrodes allow generating various types of such ‘*gap lenses*’. Here, we present the first set of measurements that validate the theoretical predictions. We performed the measurements using different photon sources, including high-harmonic generation (HHG)-based vacuum-UV, extreme-UV at the free-electron laser (FEL) FLASH and soft and hard X-ray energies at the PETRA III synchrotron (both at DESY, Hamburg). The *gap-lens-assisted extractor mode* reduces the field strength at the sample surface while increasing the diameter of the observed k -field and mitigating spherical aberration. By setting the ring electrode(s) to negative voltages, the field at the sample surface can be compensated and the *zero-field mode* can be established. It significantly improves the measurement quality for rough or 3D structured samples or devices for operando measurements with electrodes or actuators on top. Stronger negative voltages on the ring electrode enable the *repeller mode*, which removes all slow electrons below a certain kinetic energy and suppresses the main cause of the space-charge interaction.

2. Time-of-flight momentum microscopy: State-of-the-art and challenges

Time-of-flight momentum microscopy (ToF-MM) is an emerging technique, whose key advantage includes the ability to record a large (k_x, k_y, E_{kin}) parameter space without any scanning or sample rotation. Mapping out a full Brillouin zone with fixed geometry is favourable for rapid bandmapping [8] and especially for measurements of photoelectron dichroism [11] as well as spin texture [12]. The fixed geometry rules out any modulation by variation of the matrix element due to a change in angle of incidence, when rotating the crystal (like in a standard ARPES experiment).

More recently, the large phase-space acceptance has become extremely powerful for time-resolved pump-probe experiments on nonequilibrium dynamics by simultaneously capturing the dynamics of hot-electrons and holes with up to several eV above and below E_F . Since there are no review articles on this topic to-date, we will briefly summarize some recent benchmark experiments, where ToF-MM contributed substantially. Most results were generated using ToF-MMs combined with HHG sources with a few from the free-electron laser FLASH.

Among the key applications, several groups have experimentally determined the dynamics and intrinsic timescales at which phase transitions occur in materials [13-15]. Further experiments focus on the dynamics of exciton formation and retrieval of the corresponding excitonic wavefunction [16-20], including Moiré interlayer excitons in layered materials [21,22]. The experiment at FLASH exploited higher photon energies to precisely observe the correlation between core-level and conduction-band dynamics [13]. Another emerging application of ToF-MM includes ultrafast orbital tomography [23-25]. These first experiments suggest that time-resolved tomography of molecular wave functions during chemical reactions will be possible in the near future. Measurements of the 2D topological insulator bismuthene reveal interesting details on this quantum spin-Hall material [26]. Beyond the aspect of providing deep insight into photoemission dynamics, ToF-MM is especially well suited for studying time-resolved dichroism phenomena in the photoelectron patterns, as demonstrated for time-reversal and Fourier dichroism [27,28]. Theory [29] predicts Floquet physics and other light-induced topological phenomena. Time-resolved ToF-MM also sheds light on new phenomena in magnetism, including the real-time observation of the metamagnetic phase transition in FeRh [30] and phonon-electron energy flow in laser-heated Nickel [31], which employed the HEXTOF at FLASH.

Synchrotron beamlines - P04 and P22 - at PETRA III host other specialized ToF-MM instruments that can accommodate higher photon energies. Relevant recent papers focus on the rearrangement of electronic states upon Néel vector switching in the collinear metallic antiferromagnet Mn_2Au [32], and time-reversal symmetry breaking in the electronic structure of altermagnetic RuO_2 [33]. In a lab experiment using a Ti-sapphire laser, the plasmonic emission from resonantly excited nanoparticles has been studied ([34] and references therein). Examples for spin-filtered ToF-MM are given in review [35] and the application case of full-field photoelectron diffraction is discussed in [36].

A total of ~50 publications in the last three years show that ToF-MM is becoming a well-established method. However, there are several remaining challenges related to the data acquisition and control of the extractor field. First, we address the challenges arising from data

acquisition. The high data stream required to resolve simultaneously $\sim 10^7$ ‘voxels’ ($10^4 k_x, k_y$ points \times 100 energy slices) with count rates up to several 10^6 counts/second poses a large challenge. Effective data architecture and necessary controls for both hard- and software become complex due to a large amount of information needed to integrate into the data stream. State-of-the-art tr-PES experiments require a comprehensive record of all experimental parameters, including polarization states and photon energies of pump laser and probe beam, pump-probe delay, pump and probe fluences, and the spin degree of freedom in the near future. In FEL experiments, the data stream has to include specific quantities that characterize individual photon pulses, alongside with the four signals of the time-resolving detector (delay-line detector). For these reasons, we refer to this particular technique as ‘Multidimensional Photoemission Spectroscopy’. In the future, machine learning approaches can help overcome these challenges.

Second, we discuss the challenges related to the hardware of the microscope. Particularly, the high extractor voltage of the conventional cathode front lenses can cause field emission, especially for cleaved samples with sharp corners or protruding lamellae with locally-enhanced field. The only way to mitigate this problem is reducing the extractor voltage, at the expense of resolution (cf. eqs. (1-3) in [10]). In addition, an ultrafast pump-laser pulse can photoemit a large amount of slow electrons. Femtosecond pulses can induce intense electron emission from ‘hot spots’ as first observed by Fecher et al. [37]. Defects and nano-scale objects can act as plasmonic resonators that enhance the amplitude of the optical near-field by orders of magnitude, as visible in a photoemission electron microscope PEEM [38]. These resonators can emit electrons by several mechanisms [39], including near-field enhanced multi-photon photoemission (nPPE), optical field emission or single-particle decay of localized surface plasmon-polaritons.

In addition to the pump-pulse-induced slow-electron background, the secondary electrons originating from the photoemission signal of the probe pulse can contribute to space charge interaction. At low photoelectron energies, this contribution is small; however, at increasing E_{kin} , the relative amount of secondaries (in relation to the true photoelectrons) increases. Using soft-X-ray photon energies at beamline P04 at PETRA III, we observed space-charge shifts up to 10 eV in valence-band photoemission from Ir(111) at $h\nu=1000$ eV. By applying a fit using a semiempirical model [40], we revealed a total charge of the slow-electron cloud of $\sim 10^6$ e/pulse. In that case (monochromator slits were fully open) the number of secondaries exceeded the number of fast valence-band photoelectrons by 4–5 orders of magnitude (see Figs. 1 and 2 in Ref. [40]). A particularly serious scenario occurs when the pulse intensity varies, which is the case with SASE-type FELs. Then the shift varies from pulse to pulse, showing up as space-charge broadening of the signal.

To summarize, acquiring a large (k_x, k_y, E_{kin}) parameter space without sample movement and rotation significantly benefits tr-PES pump-probe experiments. Using the PEEM mode, we can identify good regions on the sample — that are free of hot spots— and optimize for the pump-probe spatial overlap (as described in Appendix A2). High quality sample regions enable stronger excitation with minimal disturbance from the space-charge effect caused by hot-spots and the extractor field. The following sections will further address these issues. Particularly, the extractor field can cause field emission or even flashovers at samples with sharp edges or protrusions. Pump laser pulses can induce slow electrons, especially from hot-

spots, that lead to energy shifts and broadening. In momentum microscopes, this is detrimental because the strong electrostatic field at the sample pulls all slow electrons into the microscope lens column. These challenges are all connected with the extractor field and urgently require alternative experimental solutions validating the predictions of [10], as described in the following sections.

The strong space-charge effects observed in previous ToF-MM experiments motivated us to perform a detailed study resulting in a semi-empirical model [40]. Based on those results, we proposed to use retarding fields to eliminate the contribution of the slow electrons to the Coulomb interaction in the beam [41, 42]. Here we introduce a new lens design sketched in Figs. 1(a-c), alongside with potential contours. It allows several modes of operation by ‘field shaping’ of the gap region between sample SA and extractor EX. The key element is the ring electrode R1, which can tailor the field in the gap. High positive potential on EX and R1 generates a strongly accelerating homogeneous field like the classical *extractor mode* (a). Setting R1 to a voltage near zero forms a ‘*gap lens*’ in front of the extractor (b) with much weaker field at the sample (*gap-lens-assisted extractor mode*). For negative voltage at R1 the field at the sample surface can be compensated (*zero-field mode*). Finally, larger negative voltages at R1 generate a retarding field at the sample (red potential contours in Fig. 1(c)) and a saddle point *S* in the potential, which acts as high-pass filter (*repeller mode*). For planar samples the *extractor mode* works well and yields high resolution. The example in (d) shows $1 \times 1 \mu\text{m}^2$ Au squares on Si, where fine structure and defects within the squares are visible; more details in Appendix 1. The *gap-lens mode* is highly attractive and was studied in all spectral ranges from $E_{\text{kin}} = 5.8 \text{ keV}$ down to 17 eV. Example (f) shows the WSe_2 valence bands; more details in Sec. 3.C. Finally, the *repeller mode* is crucial for femtosecond pump-probe experiments. It also yields higher contrast in static experiments due to the suppression of slow background electrons. Example (g) is a photoelectron diffraction pattern of Si with filigree fine structure measured in *repeller mode*; more details in Sec. 3A.

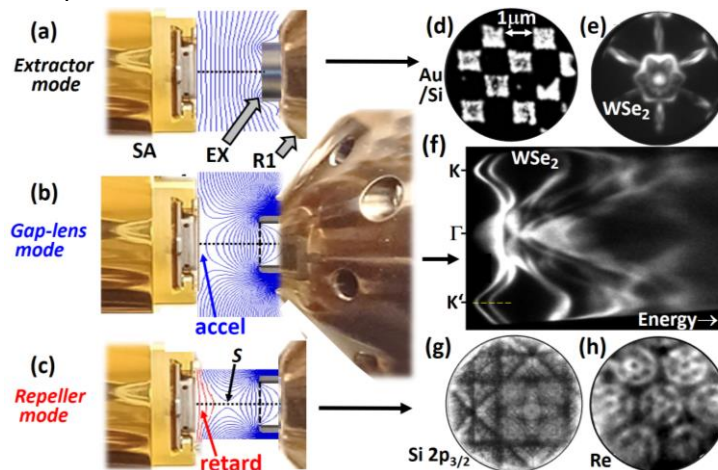


FIG. 1. Functionality of the multi-mode lens, illustrated by equipotential contours for three different modes. (a) Classical *extractor mode* with extractor and ring electrode (EX, R1) on high positive potential with respect to the sample (SA), generating a homogeneous field in the gap. (b) *Gap-lens-assisted extractor mode* with additional lens in front of the extractor (R1 at voltage near zero). The gap lens reduces the accelerating field at the sample surface, increases the *k*-field of view and mitigates spherical aberration. (c) *Repeller mode* with retarding field at the sample surface (red equipotentials) and saddle point *S*, defining the low-energy cutoff. (d-h) Examples measured for the different modes (see text).

3. Modes of the front lens in different spectral ranges

3.A Hard X-ray range

We recall that for low initial kinetic energies (typical for PEEM or LEEM experiments) the extractor field generates a virtual image of the sample with high kinetic energy E_0+eU_{extr} and small angular divergence $\alpha' = \sqrt{E_0/(E_0+eU_{\text{extr}})}\alpha_0$, where E_0 and α_0 are the emission energy and starting angle on the sample (cf. Fig. 1 in [10]). However, for electrons with several keV initial energy this picture is no longer valid because the electron-optical ‘immersion ratio’ $\sqrt{E_0/(E_0+eU_{\text{extr}})}$ approaches 1. In other words, with increasing emission energy the extractor field contribution to the total refractive power of the front lens becomes weaker and fades out at hard-X-ray energies.

We studied the influence of the extractor voltage for different initial kinetic energies between $E_0 = 1.43$ and 5.88 keV. Figure 2 shows measurements performed at beamline P22 of PETRA III (DESY). The 1st row displays the Ge 3p photoelectron diffraction patterns at photon energies of 3.28 keV (a-c) and 6 keV (d), the 2nd row the same for Si 1s at $h\nu = 3.27$ keV (e-g) and 6 keV (h). The patterns with extractor ‘on’ are shown in the 1st column, those with extractor ‘off’ (*zero-field mode*) in the 2nd and with extractor at negative potential w.r. to the sample (*repeller mode*) in the 3rd column. The settings were: $U_{\text{extr}} = 8$ kV for (a,e); $U_{\text{extr}} = U_{\text{sample}}$ for (b,f); $U_{\text{extr}} = U_{\text{sample}} - 650$ V for (c) and $U_{\text{extr}} = U_{\text{sample}} - 220$ V for (g). In all cases the (positive) sample bias was $U_{\text{sample}} = E_0/e$.

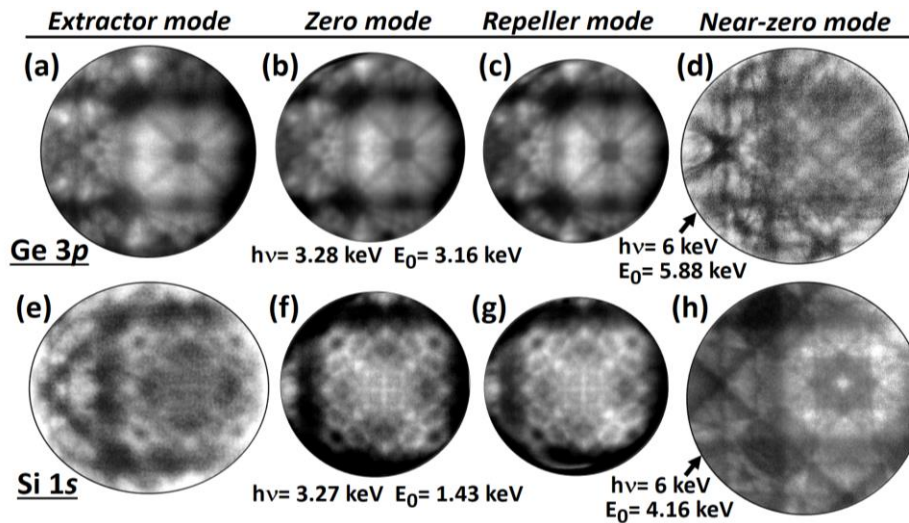


FIG. 2. Hard-X-ray photoelectron diffraction hXPD patterns of Ge 3p and Si 1s core-levels for different front-lens modes. Top row: Ge 3p hXPD pattern at an emission energy of $E_0 = 3.16$ keV recorded in *extractor* (a), *zero-field* (b) and *repeller mode* (c). (d) For $E_0 = 5.88$ keV the extractor voltage of 4.1 kV with respect to the sample has no significant effect on the patterns (*‘near-zero mode’*). Bottom row: Si 1s hXPD pattern at $E_0 = 1.43$ keV recorded in *extractor* (e), *zero-field* (f) and *repeller mode* (g). (h) Similar as (d) but for Si 1s and $E_0 = 4.16$ keV (*‘near-zero mode’*).

Comparison of the image sequences (a-c) and (e-g) reveals that the essential difference between the three modes concerns the k -field-of-view. For $E_0 = 3.16$ keV the k -FoV is reduced by 15% when switching from extractor to zero-field mode and another 5% upon further change to the *repeller* mode (a-c). For the lower initial energy $E_0 = 1.43$ keV (bottom row), the reduction is 30% when switching from *extractor* to *zero-field mode* and negligible upon further

change to the *repeller* mode (e-g). At the higher initial energies of 5.88 and 4.16 keV (d,h), there is practically no difference between the true zero mode and the *near-zero mode*, even with $U_{\text{extr}} = 10$ kV. We note that these measurements have been made using the momentum microscope located at P22 with integral dodecapole bandpass filter [43].

There is another effect alongside with the change of k -field-of-view. Close inspection of the image quality reveals that contrast and resolution increase when switching from *extractor* to *repeller mode*. Comparison of Figs. 2(e) and (g) reveal that this effect is significant at low initial energy $E_0 = 1.43$ keV. This is a characteristic of the *repeller* mode, namely stripping off all slow electrons from the photoelectron beam within a short distance from the sample surface. The retarding field in Fig. 2(g) is 200 V/mm, i.e. all electrons with kinetic energies below 100 eV are directed back to the surface within the first 500 μm above the sample surface. This means that the Coulomb interaction between the photoelectrons and the large amount of slow electrons is ‘switched off’ in the very early phase after the photon pulse. The improvement of contrast and resolution are attributed to the reduced space-charge interaction. Owing to the intrinsic Lorentzian-shaped ‘pushing’ action [40], the space-charge blur is most pronounced in the centre of the k -pattern. This is indeed visible when we compare Figs. 2(e,f,g).

We conclude that even in Synchrotron experiments with *extractor mode* the slow electrons contribute significantly to space-charge effects. In the *zero-field mode* this influence is already reduced, because only electrons within a few degrees of polar angle can enter the microscope lens column.

3.B Soft X-ray range

The soft X-ray regime comprises photon energies from ~ 100 eV to ~ 3 keV; the upper end is sometimes referred to as tender X-ray range. This energy range is nontrivial for the simulation and performance of electron optics because the ‘immersion ratio’ $\sqrt{E_0/(E_0 + eU_{\text{extr}})}$ ranges from 0.1 at 100 eV to 0.4 at 3 keV (for $U_{\text{extr}} = 15$ kV). Unlike the cases of Fig. 2, the extractor field contributes significantly to focussing and it is interesting to study the effects of the different types of gap lens on the electron distribution.

Figures 3 and 4 show two sets of data recorded at beamline P04 of PETRA III using front lenses without (Fig. 3) and with (Fig. 4) ring electrode. The image series in Fig. 3 were recorded for a SiC sample at $h\nu = 1488$ eV. The 1st row shows the result for the *long-range zero-field mode* ($U_{\text{extr}} = U_{\text{sample}}$), the 2nd row for the classical *extractor mode* ($U_{\text{extr}} = 10$ kV). The band structure of SiC is well known (see, e.g., ref. [44]); here we show these measurements only to discuss the quality of the k -patterns. Figs. 3(a-e) show (k_x, k_y) sections measured in *zero-field mode* at the binding energies indicated in the panels. We observe the prominent inner valence band head centred at the Γ -point (circular shape with slightly hexagonal warping). The valence band that is almost degenerate at the Γ -point splits in the L_1 and L_3 bands along the Γ -X direction, and the L_3 band further splits into two bands along the Γ -K direction. Figs. 3(f-j) show the same sequence measured in *extractor mode*. The observed features are the same, but they appear more blurred than in (a-e). However, the k -FoV in the *extractor mode* measurement is about a factor of 2 larger than in *zero mode*, see full FoV in Fig. 3(k). This is a result of clipping of the k -image at the hole in the extractor electrode.

The difference in contrast and resolution is even more eye-catching in the E_B -vs- k_{\parallel} sections, Figs. 3(l-o). In the patterns recorded in *zero-field mode* (l,m) the bands appear much sharper and more contrasted than for the *extractor mode* (n,o). Figure 3(l) shows the splitting of the valence band into the three L_1 and L_3 bands with increasing distance from Γ [44]. The sections (l-o) along the paths through the Γ - and K-points are marked by dashed lines in (d,i). In both sets of images the region of interest is close to the edge of the k -FoV, which accounts for the partial clipping of the patterns.

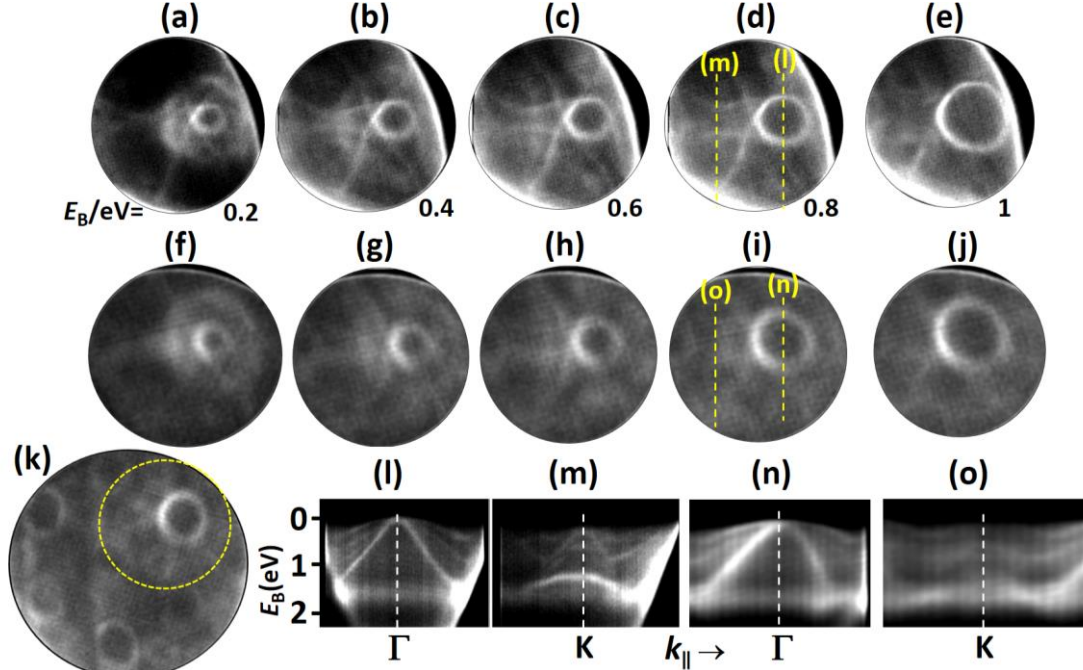


FIG. 3. Valence-band patterns of SiC measured using soft X-rays at the beamline P04 of PETRA III ($h\nu=1488$ eV). (a-e) k_x - k_y sections recorded using the *zero-field mode* with $U_{\text{extr}}=U_{\text{sample}}$; binding energies stated in the panels. (f-j) Similar data but using the *extractor mode* with $U_{\text{extr}}=10$ kV. (k) shows the full field of view in *extractor mode*, which is twice as large as for patterns (a-e), indicated by the dashed circle. (l-o) Band dispersions E_B -vs- k_{\parallel} along the dashed lines in (d,i). The better resolution and contrast in the *zero-field mode* (a-e,l,m) is evident.

The valence band results in Fig. 3 confirm our finding for core levels in Fig. 2 that the *zero-field mode* can improve the quality of the momentum patterns compared to the *extractor mode*. The number of slow electrons, which are pulled into the microscope is strongly reduced when the extractor field is switched off. In turn, the blurring of the band features due to the Coulomb interaction between the electrons is largely eliminated. The advantage of the *extractor mode* is the size of the k -field-of-view, which is about 2 times larger than in the *zero-field mode*.

Figure 4 shows data recorded at the same beamline using a front lens with ring electrode. This result has been recorded for the valence band of MoTe_2 at $h\nu=440$ eV, using the *gap-lens-assisted extractor mode* ($U_{\text{extr}}=8$ kV, $U_{\text{ring}}=0$ V). In particular, when doped with tungsten, MoTe_2 stabilizes at low temperature in the orthorhombic T_d -phase. In this phase MoTe_2 is a type-II Weyl semimetal [45], where the Weyl fermions emerge at the boundary between electron and hole pockets. Here, we show this result only to discuss the performance

of the gap-lens assisted extractor mode, further details are given in [46]. A key advantage of the *gap-lens mode* is the substantially reduced field strength at the sample surface, here 650 V/mm instead of 1520 V/mm in the typical *extractor mode* setting with $U_{\text{extr}}=U_{\text{ring}}=10\text{kV}$. In addition, the simulations predict a significantly mitigated spherical aberration. The converging gap lens with centre field strength of 1400 V/mm (see scheme in Fig. 1(b)) serves for collecting the electrons and focussing them to a k -image in the first reciprocal plane. According to the simulations [10], this k -image shows much lower spherical aberration compared with the extractor mode. The central question of this study was whether the excellent imaging properties predicted by ray tracing can actually be experimentally confirmed.

Fig. 4(a) shows a k_x - k_y section at the Fermi energy. We observe a periodic pattern reflecting the repeated Brillouin zones with the band heads of the valence bands and the band minima of the conduction bands close to the Γ -points (elongated along the Γ -Y direction). The rectangular Brillouin zone with high symmetry points is indicated. Figs. 4(b,c) show E_B -vs- k_{\parallel} sections along the X- Γ -X and Y- Γ -Y lines, respectively. The band heads appear sharp, and the fine structure of several bands is clearly visible. Furthermore, contrast and resolution remain consistently good along the sequence of 5 adjacent Γ -points in Fig. 4(b). We can conclude at this point: The electric field at the sample surface for the present setting of the *gap-lens-assisted extractor mode* is about a factor of 2 lower than for an equivalent conventional *extractor mode*. Moreover, the momentum pattern exhibits an excellent quality, which confirms the performance expected from the simulations.

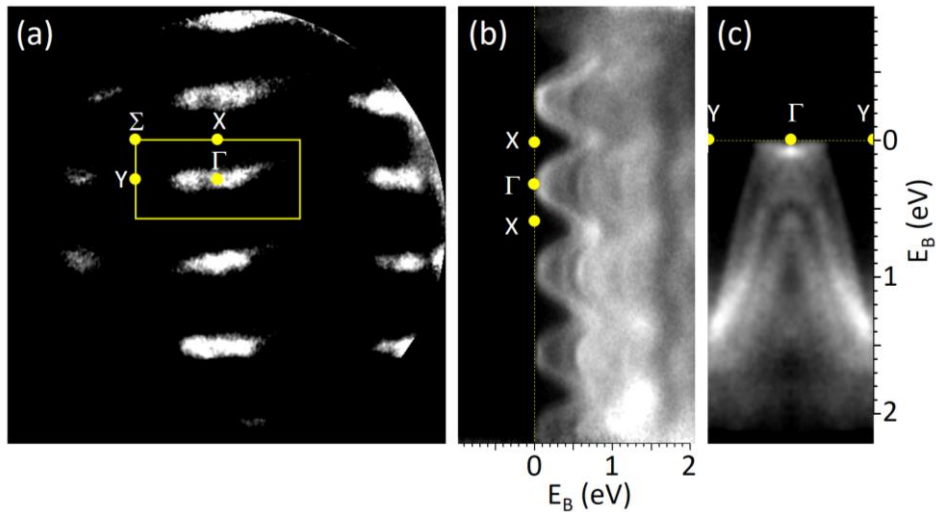


FIG. 4. Valence-band pattern of MoTe_2 recorded at beamline P04 ($h\nu= 440$ eV) using the *gap-lens-assisted extractor mode* ($U_{\text{extr}}= 8$ kV; $U_{\text{ring}}= 0$ V). (a) k_x - k_y section at the Fermi energy; (b,c) E_B -vs- k_{\parallel} sections along the X- Γ -X and Y- Γ -Y lines, respectively. A key advantage of this mode is the significantly reduced field strength at the sample surface (here 650 V/mm), mitigating the risk of field emission at defects or protrusions.

3.C Low-energy range (HHG)

The low-energy regime is of high interest to many laboratory setups that host ToF-MMs combined with HHG-based XUV sources for investigation of ultrafast light-induced dynamics using pump-probe techniques [14-23,25-28]. Photoelectron energies E_0 typically lie in the range of ~ 17 to >40 eV. This energy range falls below the cutoff energy in the *repeller mode* for the soft- and hard-X-ray regimes. The close vicinity of the cutoff energy and the photoelectron energy makes the low-energy case much more demanding. From an electron-optical point of view setting the cutoff of the undesired slow electrons so close to the signal of interest is quite critical. Here, we show first results with the *gap-lens* and *repeller modes*. More systematic studies are underway to elucidate the limits of the *repeller mode* for low-energy electrons.

The first experiments using the ToF-MM with HHG-based XUV source at Centre Lasers Intenses et Applications (CELIA), in Bordeaux (France) revealed very positive results using the *gap-lens-assisted extractor mode*. The key element is an accelerating converging lens in the gap between the sample and extractor (Fig. 1(b)), generated by the ring electrode. This gap lens replaces the strong extractor field of the conventional mode. Simulations suggested several advantages: (i) The electric field at the sample surface is typically a factor of 2 smaller than in the extractor mode without the gap lens. This is beneficial because it eliminates the risk of field emission or flashovers for samples with sharp corners or protrusions. (ii) The collection efficiency is even higher than with a full extractor field. Therefore, larger k -fields can be imaged at identical settings of the downstream lenses. (iii) Last but not least the spherical aberration, in particular the field curvature, is substantially reduced and the depth of focus is enhanced (simulations are shown in ref. [10]).

Figure 5 shows a measurement for a cleaved bulk 2H-WSe₂ sample (at room temperature) using femtosecond XUV pulses (photon energy 21.6 eV, repetition rate 166 kHz, pulse duration ~ 100 fs). Here the extractor was at 8 kV and the ring electrode at -2 kV, which reduces the field strength at the sample surface to 550 V/mm. In the center of the gap lens the field is 1530 V/mm, in other words this is a strong converging lens. With both electrodes at 8 kV the field at the sample would be 1250 V/mm. The k_x - k_y (a-f) and E_B - k_x sections (g-i) are rich in details. The k_x - k_y cuts (a-f) cover a large energy range of ~ 6 eV from the top of the valence band to close to the bottom of the valence band; binding energies are stated in panels. Sections (g) and (h) run along the K- Γ -K' and K-M-K' lines, respectively. Section (i) runs parallel to K-M-K' but somewhat shifted towards the Γ -point. Close inspection reveals that in (i) a hybridization gap (avoided crossing) opens, marked by an arrow. Contrast and resolution in this k -pattern are high, so that this local bandgap of <100 meV width is clearly visible. (j) shows an intensity line scan along the dashed line at the K-point in (g), revealing a width of the bands of 100 meV FWHM. We see essentially the thermal broadening at room temperature; the optical bandwidth of the VUV-beam is 40 meV.

Figure 6 shows a measurement at the same settings but for the *repeller mode* ($U_{\text{extr}}=4.5$ keV; $U_{\text{ring}}=-5.5$ keV). Here the field at the sample surface was -10 V/mm, which redirects all electrons with kinetic energies < 5 eV within the first 500 μm above the sample surface. The saddle point of the potential (defining the cutoff) is at about 12 eV and further

downstream the converging gap lens serves for image formation (Fig. 1(c)). The k_x - k_y section (a) reveals that the k -field-of-view is reduced by $\sim 50\%$ at the valence-band maximum. The E_B - vs - k_{\parallel} sections (b) and (c) are shown along the K- Γ and K-M-K' lines, respectively. Towards lower kinetic energy the horizon shrinks further and finally the image contracts to a bright spot upon approaching the cutoff energy.

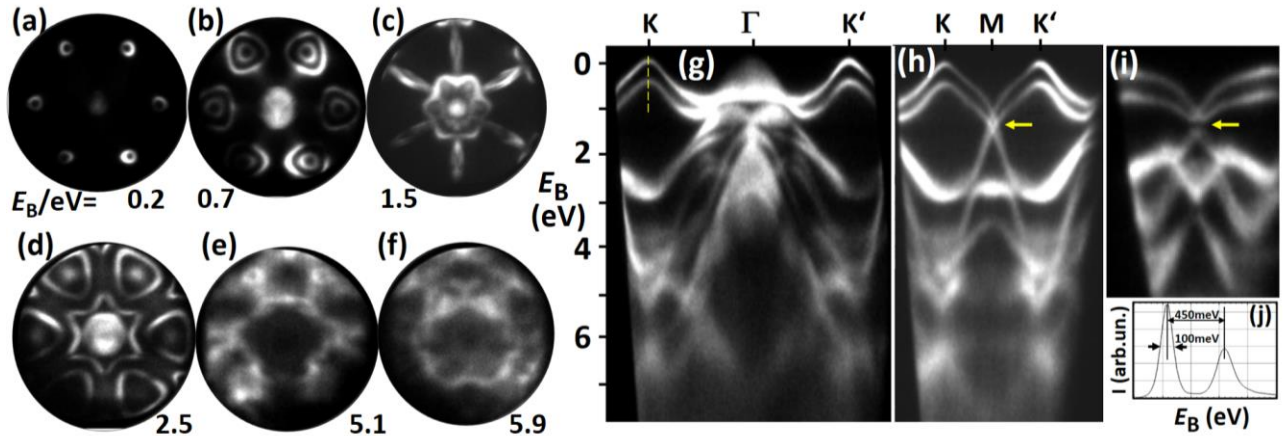


FIG. 5. Measurement using the *gap-lens-assisted extractor mode* at low energy ($h\nu = 21.6$ eV) ($U_{\text{extr}} = 8$ kV; $U_{\text{ring}} = -2$ kV), performed using the ToF-MM at the HHG source at CELIA, Bordeaux. This mode is characterized by a reduced electric field at the sample surface (here +550 V/mm), higher collection efficiency and lower spherical aberration (field curvature). (a-f) k_x - k_y sections at binding energies E_B as stated. (g-i) E_B - vs - k_x sections along K- Γ -K', K-M-K' and parallel to K-M-K', respectively. The arrows mark an avoided crossing of the spin-orbit split top band close to the M point. (j) Intensity line scan along the dashed line in (g).

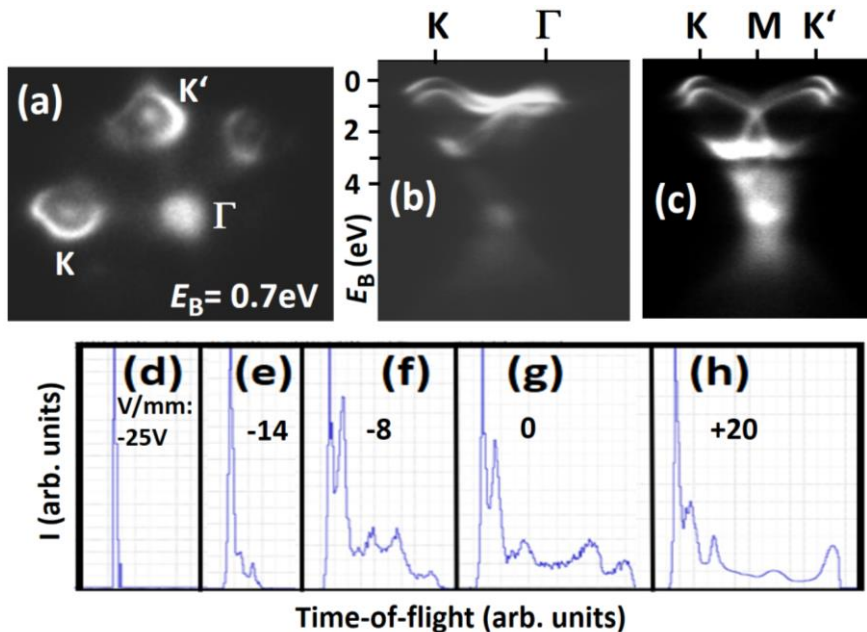


FIG. 6. Measurement like Fig. 5 but using the *repeller mode* ($U_{\text{extr}} = 4.5$ kV, $U_{\text{ring}} = -5.5$ kV; retarding field at the sample surface -10 V/mm). (a) k_x - k_y section at a binding energy of 0.7 eV. (b,c) E_B - vs - k_{\parallel} sections along the K- Γ and K-M-K' lines, respectively. (d-h) Sequence of ToF spectra as function of the field at the sample surface (values stated in panels), set by variation of U_{ring} .

Figures 6(d-h) show the cutoff behaviour in terms of the transmitted ToF spectra as function of the repeller field. At -25V/mm just the top valence band can pass (d). Upon reducing the field, the lower-lying bands appear (e-g). Finally at positive field the full spectrum is transmitted (h). Several comments are important at this point: A kinetic energy of $E_0= 17$ eV is the extreme case. From the simulations [10] it is evident that this energy is very close to the limit, where the repeller principle breaks down. The result of Fig. 6 is the first measurement at such low energies using this mode, following the earlier measurements at FLASH [42] at $E_0= 107$ eV. Further systematic studies are in progress, in order to elucidate the desired effect of this mode - the space-charge suppression effect. Cutting off the low energy electrons has a practical drawback: It is not possible to see the pump spot in this mode. Pump-probe overlap needs to be adjusted in one of the other modes (e.g. the *gap-lens-assisted extractor mode*) before switching to the *repeller mode* for the k -measurement. When extractor and ring electrode are set to high positive potential (classical *extractor mode*), the new lens geometry yields very good performance in standard PEEM operation, see examples in Appendix A.

3.D ToF-XPEEM real-space imaging with sub-micron resolution

In the previous sections, we have addressed the k -imaging modes. Now we consider real-space imaging at higher energies with element selectivity, i.e. imaging on a core-level signal. Unlike threshold PEEM, where the image contrast originates from workfunction variations or topographic features, the image is formed by chemical contrast in case of XPEEM. The higher kinetic energy poses a challenge for the lateral resolution.

Let us consider an extreme case in the hard X-ray range. Momentum microscopy has been able to perform up to kinetic energies of $E_0= 7$ keV [47]. In which, the aberration terms increase while the ratio E_0 / eU_{extr} approaches one with increasing E_0 . On the other hand, the angular range of interest becomes very small. At 7 keV, a k -field diameter of 12 \AA^{-1} (consisting of many Brillouin zones [48]) corresponds to a polar angular range of only $0 - 4^\circ$. For a gap of $\ell = 6$ mm, $U_{\text{extr}} = 14$ kV, and $\alpha_0= 4^\circ$, eq. (1) in [10] predicts $\delta_{\text{S,acc}} \approx 2 \text{ \mu m}$ for the spherical aberration in PEEM mode. In the measurement reported in Ref. [47], the energy width of a narrow core level is given by the monochromator bandwidth ≈ 600 meV. We obtain $\delta_{\text{C,acc}} \approx 4.5 \text{ \mu m}$ for the chromatic aberration and a total aberration of the acceleration field of $\sqrt{(\delta_{\text{S,acc}})^2 + (\delta_{\text{C,acc}})^2} \approx 5 \text{ \mu m}$. Hence, in order to perform X-PEEM with sub- μm resolution, the angular range needs to be confined by a contrast aperture.

We demonstrated the new technique of ToF-XPEEM first on a test sample (Chessy Plano GmbH), followed by a 2D semiconductor using soft X-rays at beamline P04 of PETRA III. The goal was to demonstrate X-ray element-selective, spectra-imaging real space measurements. Figs. 7(a,b) show measurements on the test sample (hierarchical checkerboard pattern of Au on Si, for details, see Appendix A1) at the Au $4f$ and Si $2p$ core levels. The image recorded on Au $4f_{7/2}$ (a) shows the pattern, where the $10 \times 10 \text{ \mu m}^2$ Au squares form the macroscopic checkerboard. The corresponding image on the Si $2p$ core-level signal is shown in Fig. 7(b). These images are formed by chemical contrast, as visible in the pattern of bright squares when imaging on the Au core level (a) and the inverted contrast on the Si line (b), showing the regions not covered by Au. Each of the $10 \times 10 \text{ \mu m}^2$ Au squares consists of $1 \times 1 \text{ \mu m}^2$

squares. The line scan close to the corner of a $10 \times 10 \mu\text{m}^2$ square (marked by a line in (a)) reveals the profile of these $1\text{-}\mu\text{m}$ squares (Fig. 7(i)), providing a ruler for the lateral scale.

Next, we used ToF-XPEEM to characterize the spatial distribution and spectroscopic signatures of p-type Vanadium dopant within the 2D semiconductor WS_2 , Figs. 7(c-e). Multilayer WS_2 islands ranging from $3\text{-}20 \mu\text{m}$ in lateral size are grown via metal-organic chemical vapor deposition, with nominal vanadium dopant concentrations of 30 atom%. The measurements reveal unique elemental spectroscopic signatures, including chemical shifts, that reflect the stoichiometry within each island. The spatial maps unravel the atomic positions of Vanadium and Tungsten within the 2D flakes [49]. We acquired images first without contrast aperture, Fig. 7(c), and then with a contrast aperture of dia. $300 \mu\text{m}$ in the backfocal plane of the front lens, Figs. 7(d,e).

The improvement of spatial resolution for this ‘real’ system upon insertion of a contrast aperture is striking: The line scans marked in (d,e) reveal a width of 0.65 and $0.77 \mu\text{m}$ (FWHM), Fig. 7(j,k). The corresponding ToF spectra with marked working points are shown in (f-h). The working points and kinetic energies are stated in the panels, the energy scale is slightly non-linear. The scale bar in (f) refers to the center of the panels; the spin-orbit splittings are 3.6 eV for Au $4f$ and 2.2 eV for W $4f$.

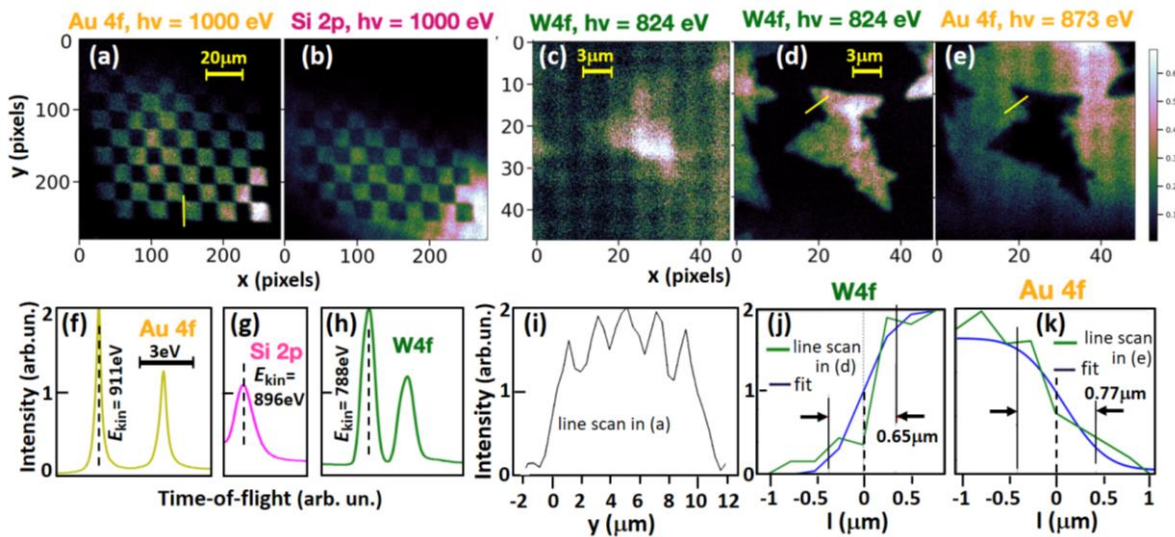


FIG. 7. Real-space measurements (ToF-XPEEM) in the soft-X-ray range using the *gap-lens-assisted extractor mode*. (a,b) Element-resolved imaging of a test sample (Au checkerboard pattern on Si; Chessy, Plano GmbH) at $h\nu = 1000 \text{ eV}$. Images on the (a) Au $4f_{7/2}$ and (b) Si $2p$ core-level signals show reversed contrast. (c-e) Similar measurement on Vanadium-doped WS_2 flakes on Au, (c) without and (d,e) with contrast aperture. The gain in spatial resolution is dramatic. Images (a-e) were recorded in 15 minutes at $T = 30 \text{ K}$. (f-h) Corresponding ToF spectra of the Au $4f$, Si $2p$ and W $4f$ core-levels, respectively. The working points are marked by dashed lines. (i) Intensity line-profile along the edge of one of the $10 \times 10 \mu\text{m}^2$ squares, marked in (a). The row of $1 \times 1 \mu\text{m}^2$ squares is partially resolved, serving as ruler for the lateral scale. (j,k) Measured line-profiles (red) across the corner of the central flake as marked in (d,e). Blue curves result of a fit, revealing resolution values of 0.65 and $0.77 \mu\text{m}$ (FWHM) in the W $4f$ and Au $4f$ images, respectively.

Close inspection of our raw data revealed that the measurements of Fig. 7(a,b,d,e) are limited by the pixel resolution of the detector (1240 pixels along the image diameter). In order to reach the ultimate resolution it will be necessary to zoom in towards larger magnification.

The chromatic aberration of magnification can easily be corrected numerically [50]. Under the given conditions (peak widths ~ 0.3 eV and ~ 0.5 eV FWHM for Au and W, respectively) this effect is still negligible. We note that the HAXPEEM [51] has demonstrated a resolution of 300 nm and nano-ARPES with zone-plate optics achieves values of 120 nm in scanning mode [52]. The main advantages of the ToF method are the high count rate thanks to parallel energy recording and easy switch between real-space and k -space imaging. The images in Figs. 7(a-e) were taken in 15 minutes. The Au square patterns and WS₂ flakes on the Au and W 4f signals were already visible in real-time imaging at a frame rate of 1/s. The base resolution of the microscope with the new front lens in *extractor mode* is in the range of 50 nm, cf Appendix A.

4. Conclusions and Outlook

The design criteria of cathode-lens microscopes, which record photoelectron emission patterns in real or momentum space, are governed by the paradigm that good instrument performance requires a strong accelerating electric field (extractor field) in front of the sample. The key advantage of the extractor field is the large accessible interval of energy-momentum space. When combined with ToF energy recording, momentum microscopes can record up to 10^7 (k_x, k_y, E_{kin}) data voxels simultaneously, without scanning or sample rotation.

This large phase-space acceptance has some drawbacks. Unwanted slow background electrons are pulled into the microscope column, where they can dramatically increase space-charge shifts and broadening. Another problem associated with the extractor field is the risk of field emission or even flashovers at sharp corners or local protrusions, e.g. of cleaved samples. The common way of overcoming this problem is to reduce the extractor voltage, which comes at the expense of a loss of resolution. Here we have presented an alternative route to good performance in k -imaging mode, which is based on ‘field shaping’ in the region close to the sample. This is made possible by a new front lens architecture with an additional ring-shaped lens element concentric to the extractor electrode. By applying different voltages to the ring electrode, different types of lenses can be created in the gap between the sample and the first electrode. These *gap lenses* are associated with different fields on the sample surface (accelerating, zero or decelerating). If there are no problems with the high extractor field and no significant background of slow electrons the extractor mode is fine.

The main objectives of the present studies were: (i) validate electron-optical predictions [10] for k -imaging with reduced field strength at the sample surface. (ii) Extend previous space-charge suppression strategies to the lower energies of HHG-based experiments. (iii) Conduct a first pilot study on how the new lens modes affect real-space imaging in X-PEEM mode. The different modes of operation have been studied over a wide spectral range, including energies from the soft and hard X-ray range (up to $h\nu = 6$ keV) at the synchrotron source PETRA III, Hamburg, down to the VUV range ($h\nu = 21.6$ eV) at the HHG-based ToF-MM at CELIA, Bordeaux. The results showed that the electric field on the sample can be reduced by a factor of 2 by proper setting of the *gap lens* and the large amount of unwanted slow electrons can be removed from the beam in the *zero-field* and *repeller modes*.

The *zero-field* and *gap-lens-assisted extractor modes* showed excellent performance over all spectral ranges. At energies between 5.8 and 1.4 keV we found evidence of an improved quality of the k -images, when changing from *extractor* to *zero mode* (Figs. 2 and 3). We

attribute this to the ‘switching off’ of most of the space-charge interaction between photoelectrons and slow background electrons. We have ensured that this advantage persists down to lower energies in the soft-X-ray range (see result at 440 eV in Fig. 4). Real-space imaging also benefits from the new lens modes as we confirmed by ToF-XPEEM imaging with 650 nm resolution (Fig. 7).

This development was fuelled by the recent success of ToF momentum microscopy for the investigation of ultrafast phenomena using pump-and-probe techniques [13-31]. The results for an emission energy of $E_0=17$ eV (Figs. 5,6) are of central importance as an extension of the previous pilot study with the HEXTOF at FLASH at $E_0=107$ eV [42]. At this low energy, however, it is no longer possible to simultaneously record a complete Brillouin zone, since the use of the *repeller mode* is associated with a reduction of the k -field-of-view by about a factor of 2. This reduction will be less severe for ToF-MMs at future HHG-based sources with photon energies in the range ≥ 100 eV, which will benefit strongly from the different modes. More systematic work is needed to clarify the final limits of the method at low energies. Future goals concern the possibility of 4D (k_x, k_y, k_z, E_{kin}) recording by exploiting the curvature of the photoemission final-state sphere in k -space, as shown in [53]. The first ToF X-PEEM results (Fig. 7) suggest further advantages of the *gap-lens modes*, in particular for fs time-resolved PEEM [54]. Last but not least, the implementation of spin resolution [55] in tr ToF-MM will benefit from space charge suppression, since spin detection is associated with a strong loss of recording efficiency.

Acknowledgements

We acknowledge DESY (Hamburg, Germany), a member of the Helmholtz Association HGF, for the provision of experimental facilities. Parts of this research were carried out at PETRA III, beamlines P04 and P22. We further acknowledge funding from CNRS, Université de Bordeaux and Quantum Matter Bordeaux. Instrument at CELIA funded by the European Union. Views and opinions expressed are those of the authors only and do not necessarily reflect those of the European Union. Neither the European Union nor the granting authority can be held responsible for them. Work in Mainz was funded by Bundesministerium für Bildung und Forschung BMBF (Projects 05K22UM1 and 05K22UM2) and Deutsche Forschungsgemeinschaft DFG through Transregio SFBs Spin+X TRR175-268565370 (project A02) and Elasto-Q-Mat TRR288-422213477 (project B04).

Q.N. acknowledges support by the SLAC-Stanford Quantum Initiative Q-FARM Bloch Fellowship and U.S. DOE (DE-AC02-76SF00515). J.A.S. was supported by the U.S. Department of Energy, Office of Basic Energy Sciences, Division of Materials Science and Engineering under contract DE-AC02-76SF00515. J.D.K. was funded by the Linac Coherent Light Source (LCLS), SLAC National Accelerator Laboratory, U.S. Department of Energy, Office of Science, Office of Basic Energy Sciences under Contract No. DE-AC02-76SF00515

Sincere thanks go to Andrew J. Mannix, Zhepeng Zhang, Lauren Hoang and Eric Pop (Stanford University, USA) for providing the Vanadium-doped WS₂ samples and to Martina Müller (Konstanz University, Germany) for a critical reading of the manuscript.

Data availability

All data shown within this article is available on reasonable request. The authors declare no competing interests.

APPENDIX

A.1 Performance of the multi-mode lens in UV PEEM with *extractor mode*

Prior to the HHG-based experiments (Sec. 3.C) we tested the new lens with ring electrode using UV-PEEM imaging in normal *extractor mode* ($U_{\text{extr}} = U_{\text{ring}} = 12$ kV). A series of images with different lateral magnification and different sizes of field apertures is shown in Fig. A1. (a-f) show fields of views between 600 and 15 μm as stated. As excitation sources we used a Hg lamp (a,d,e) and a UV-LED (b,c,f). The Hg lamp has a quite broad spectral distribution centered at $h\nu = 4.9$ eV, whereas the UV-LED produces a sharp line at 4.6 eV. This different spectral character is visible in the PEEM images: The Hg lamp yields rather homogeneously-looking images of the Au checkerboard pattern (e.g. (e)), whereas the UV-LED with the lower energy and sharp line emphasizes microscopic defects and fine structure in the Au squares on a large (b) and small (f) length scale. A line scan across one of the $1 \times 1 \mu\text{m}^2$ squares in Fig. A1(f) reveals a resolution of 50 nm. This is not the ultimate resolution because of the 3D structure of the Chessy test object. In Fig. A1(d) the auxiliary grid in the first intermediate image (plane of the field apertures) is inserted. The superposition of the image of the sample with the sharp shadow pattern of the grid serves as a means for fast adjustment of Gauss images.

Figures A1(g-k) show regions-of-interest (ROIs) defined by field apertures with different sizes between 9 μm and 500 nm. The dashed circles mark the sizes of the field apertures. The checkerboard pattern provides a ruler for the actual size of the ROIs on the sample surface. The lateral magnification of the intermediate image is ~ 10 , i.e. the actual apertures are 10x larger than the ROIs (the smallest aperture was 5 μm , used for (k)). Note that this microscope enables sub-micron ROIs just by introducing small apertures in the intermediate image plane. This mode allowed us to observe individual antiferromagnetic domains in Mn_2Au [56].

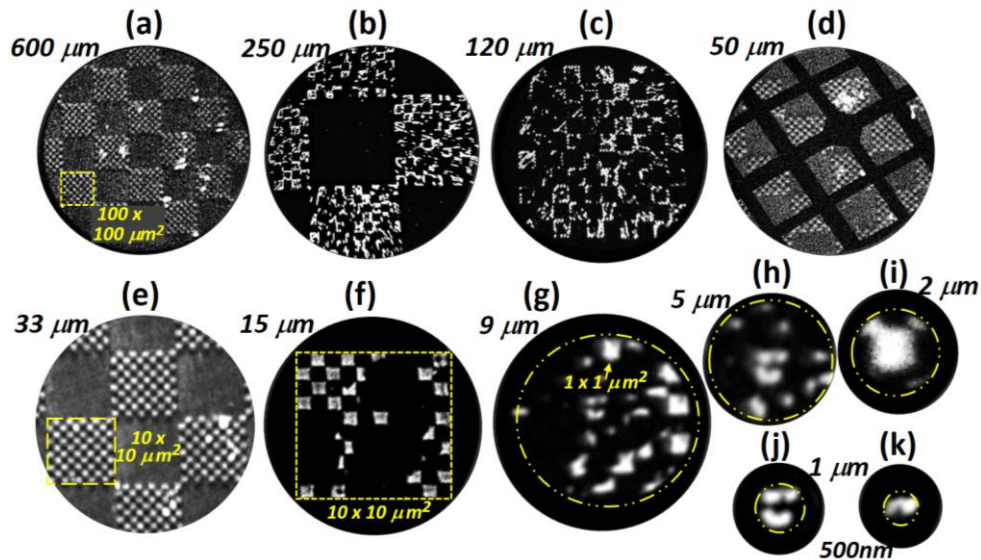


FIG. A1. Real-space imaging (UV-PEEM) using the *extractor mode* ($U_{\text{extr}} = U_{\text{ring}} = 12$ kV). (a-f) Series of images of a test sample (Au checkerboard pattern on Si; Plano GmbH) at different magnifications, quantified by the field of view between 600 and 15 μm as stated in the panels. (a,d,e) were taken using a Hg lamp ($h\nu = 4.9$ eV), (b,c,f) using a UV-LED ($h\nu = 4.6$ eV). In the latter case the checkerboard pattern emits rather inhomogeneously. In (d) the auxiliary grid (diagonal grid pattern) in the first intermediate image plane was introduced, which facilitates easy adjustment of Gauss images. (g-k) Measurements series using field apertures for selection of small regions of interest (ROIs), here between 9 μm and 500 nm as stated in the panels.

A.2 Preparing pump-probe measurements when *hot spots* are present

Fig. A2 illustrates a typical situation when searching for a ‘good spot’ on a cleaved sample (here bulk 2H-WSe₂) in a pump-probe experiment using infrared femtosecond pulses as pump and VUV pulses produced by HHG as a probe. Using the PEEM mode and large-area illumination by a UV-LED (Fig. A2(a)), we centre a homogeneously-looking region (here in the upper part) on the detector. Next, we take images with the infrared pump beam (photon energy 1.2 eV, repetition rate 166 kHz) alone (b,c). Initially, two strong hot spots are located at the rim of the field of view (FoV), where their intensities dominate the pump-beam pattern (b). By shifting the sample and slightly refocussing, we drive the hot spots out of the FoV to make the footprint of the *pump* beam visible (c). Next, we centre the *probe* beam (photon energy 21.6 eV) onto the same position as the pump (d). Illuminating with pump and probe beam simultaneously enables optimization of their spatial overlap. Figure A2(e) shows the spatially overlapped *pump-and-probe* pattern. Finally, we place a *field aperture* (here corresponding to ~20 μm dia. on the sample surface) at the centre of the pump-and-probe pattern (f). Images (b-f) are measured time-resolved at the low-energy cutoff of the spectra. This was the starting condition before acquisition of *k*-measurements shown in Sec. 3.C.

Since hot spots act as resonantly-excited plasmonic antennas, their local electron yield can exceed the photoelectron signal from the probe pulse by orders of magnitude. Electrons from hot spots have low E_{kin} , so the extractor field pulls them into the microscope column, where they contribute to the space-charge interaction with the photoelectrons. Figure A2(b) reveals that even the low photon intensity in the rim of the pump pulse can be sufficient to excite large electron signals from hot spots. In addition, the hot-spot emission from regions outside of the field-of-view of the PEEM image (in Fig. A2 dia. 250 μm) contributes to the space-charge effect.

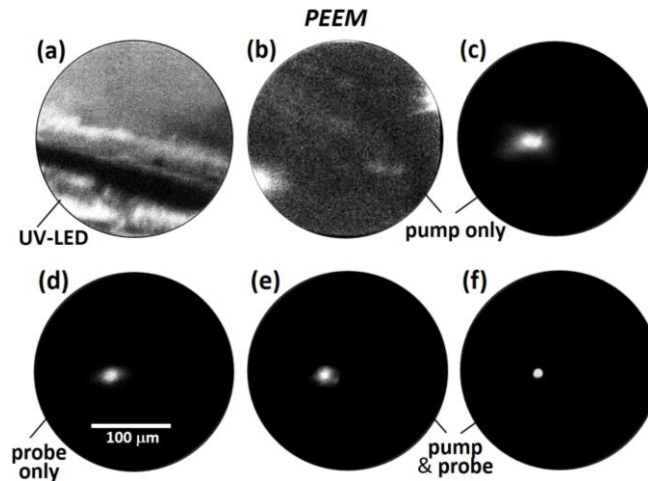


FIG. A2. Sequence of real-space images (PEEM-mode; field-of-view ~250 μm) prior to a *k*-mode measurement. (a) PEEM image of the cleaved WSe₂ sample with illumination by a UV-LED (4.6 eV, cw). (b) Image recorded with pump pulse only (1.2 eV, ~130 fs) on a smooth-looking sample position exhibiting two strong emission regions (‘hot spots’) at the rim. (c) Same after moving the sample and slight refocussing of the pump beam. (d) Image recorded with probe pulse only (21.6 eV, ~100 fs) after aligning its position to the same spot. (e) Image recorded with pump and probe pulse. (f) Same after placing a field aperture to the intensity maximum for precise definition of the probe area (dia. 20 μm).

References

- [1] M. Kotsugi, W. Kuch, F. Offi, L.I. Chelaru and J. Kirschner, **Microspectroscopic two-dimensional Fermi surface mapping using a photoelectron emission microscope**. Rev. Sci. Instrum. **74** (2003) 2754-2758; doi:10.1063/1.1569404
- [2] B. Krömker, M. Escher, D. Funnemann, D. Hartung, H. Engelhard and J. Kirschner, **Development of a momentum microscope for time resolved band structure imaging**, Rev. Sci. Instrum. **79**, 053702 (2008); doi:10.1063/1.2918133
- [3] C. Tusche, A. Krasnyuk and J. Kirschner, **Spin resolved bandstructure imaging with a high resolution momentum microscope**, Ultramicroscopy **159**, 520 (2015); doi:10.1016/j.ultramic.2015.03.020
- [4] S. Suga and C. Tusche, **Photoelectron spectroscopy in a wide hv region from 6 eV to 8 keV with full momentum and spin resolution**, J. Electron Spectrosc. Relat. Phenom. **200** (2015) 119; doi: 10.1016/j.elspec.2015.04.019
- [5] G. Schönhense, S. Babenkov, D. Vasilyev, H.-J. Elmers and K. Medjanik, **Single-Hemisphere Photoelectron Momentum Microscope with Time-of-Flight Recording**, Rev. Sci. Instrum. **91**, 123110 (2020); doi: 10.1063/5.0024074
- [6] F. Matsui, K. Hagiwara, E. Nakamura, T. Yano, H. Matsuda, Y. Okano, S. Kera, E. Hashimoto, S. Koh, K. Ueno, T. Kobayashi, E. Iwamoto, K. Sakamoto, S.-I. Tanaka and S. Suga, **Soft x-ray photoelectron momentum microscope for multimodal valence band stereography**, Rev. Sci. Instrum. **94**, 083701 (2023); doi:10.1063/5.0154156
- [7] M. Schmitt, D. Biswas, O. Tkach, J. Liu, O. Fedchenko, H. J. Elmers, M. Sing, R. Claessen, G. Schönhense and T.-L. Lee, in preparation
- [8] K. Medjanik, O. Fedchenko, S. Chernov, D. Kutnyakhov, M. Ellguth, A. Oelsner, B. Schönhense, T. R. F. Peixoto, P. Lutz, C.-H. Min, F. Reinert, S. Däster, Y. Acremann, J. Vieffhaus, W. Wurth, H. J. Elmers and G. Schönhense, **Direct 3D Mapping of the Fermi Surface and Fermi Velocity**, Nature Materials **16**, 615 (2017)
- [9] D. Kutnyakhov, P. Xian, M. Dendzik, M. Heber, F. Pressacco, S.Y. Agustsson, L. Wenthaus, H. Meyer, S. Gieschen, G. Mercurio, A. Benz, K. Bühlman, S. Däster, R. Gort, D. Curcio, K. Volckaert, M. Bianchi, Ch. Sanders, J.A. Miwa, S. Ulstrup, A. Oelsner, C. Tusche, Y.J. Chen,, D. Vasilyev, K. Medjanik, G. Brenner, S. Dziarzhyski, H. Redlin, B. Manschwetus, S. Dong, J. Hauer, L. Rettig, F. Diekmann, K. Rossnagel, J. Demsar, H.J. Elmers, P. Hofmann, R. Ernstorfer, G. Schönhense, Y. Acremann and W. Wurth, **Time- and momentum-resolved photoemission studies using time-of-flight momentum microscopy at a free-electron laser**, Rev. Sci. Instrum. **91**, 013109 (2020); doi: 10.1063/1.5118777
- [10] O. Tkach and G. Schönhense, **Multi-Mode Front Lens for Momentum Microscopy: Part I Theory**
- [11] O. Fedchenko, K. Medjanik, S. Chernov, D. Kutnyakhov, M. Ellguth, A. Oelsner, B. Schönhense, T. Peixoto, P. Lutz, C.-H. Min, F. Reinert, S. Däster, Y. Acremann, J. Vieffhaus, W. Wurth, J. Braun, J. Minár, H. Ebert, H. J. Elmers and G. Schönhense, **4D texture of circular dichroism in soft-x-ray photoemission from tungsten**, New J. of Phys. **21**, 013017 (2019); doi: 1367-2630/aaf4cd
- [12] G. Schönhense, K. Medjanik, S. Chernov, D. Kutnyakhov, O. Fedchenko, M. Ellguth, D. Vasilyev, A. Zaporozhchenko, D. Panzer, A. Oelsner, C. Tusche, B. Schönhense, J. Braun, J. Minár, H. Ebert, J. Vieffhaus, W. Wurth and H. J. Elmers, **Spin-Filtered Time-of-Flight k-Space Microscopy of Ir – Towards the “Complete” Photoemission Experiment**, Ultramicroscopy **183**, 19–29 (2017); doi: 10.1016/j.ultramic. 2017.06.025
- [13] M. Dendzik, R. P. Xian, E. Perfetto, D. Sangalli, D. Kutnyakhov, S. Dong, S. Beaulieu, T. Pincelli, F. Pressacco, D. Curcio, S. Y. Agustsson, M. Heber, J. Hauer, W. Wurth, G. Brenner, Y. Acremann, P. Hofmann, M. Wolf, A. Marini, G. Stefanucci, L. Rettig and R. Ernstorfer, **Observation of an Excitonic Mott Transition Through Ultrafast Core-cum-Conduction Photoemission Spectroscopy**, Phys. Rev. Lett. **125**, 096401 (2020); doi:10.1103/PhysRevLett.125.096401

- [14] S. Beaulieu, S. Dong, N. Tancogne-Dejean, M. Dendzik, T. Pincelli, J. Maklar, R. P. Xian, M. A. Sentef, M. Wolf, A. Rubio, L. Rettig and R. Ernstorfer, **Ultrafast dynamical Lifshitz transition**, *Science Adv.* **7**, eabd9275 (2020)
- [15] S. Dong, S. Beaulieu, M. Selig, P. Rosenzweig, D. Christiansen, T. Pincelli, M. Dendzik, J. D. Ziegler, J. Maklar, R. P. Xian, A. Neef, A. Mohammed, A. Schulz, M. Stadler, M. Jetter, P. Michler, T. Taniguchi, K. Watanabe, H. Takagi, U. Starke, A. Chernikov, M. Wolf, H. Nakamura, A. Knorr, L. Rettig and R. Ernstorfer, **Observation of ultrafast interfacial Meitner-Auger energy transfer in a van der Waals heterostructure**, *Nat. Commun.* **14**, 5057 (2023)
- [16] J. Madéo, M. K. L. Man, C. Sahoo, M. Campbell, V. Pareek, E. L. Wong, A. Al-Mahboob, N. S. Chan, A. Karmakar, B. M. K. Mariserla, X. Li, T. F. Heinz, T. Cao and K. M. Dani, **Directly visualizing the momentum-forbidden dark excitons and their dynamics in atomically thin semiconductors**, *Science* **370**, 1199 (2020)
- [17] R. Wallauer, R. Perea-Causin, L. Münster, S. Zajusch, S. Brem, J. Gütde, K. Tanimura, K.-Q. Lin, R. Huber, E. Malic and U. Höfer, **Momentum-Resolved Observation of Exciton Formation Dynamics in Monolayer WS₂**, *Nano Letters* (2021); doi:10.1021/acs.nanolett.1c01839
- [18] M. K. L. Man, J. Madéo, C. Sahoo, K. Xie, M. Campbell, V. Pareek, A. Karmakar, E. Laine Wong, A. Al-Mahboob, N. S. Chan, D. R. Bacon, X. Zhu, M. M. M. Abdelrasoul, X. Li, T. F. Heinz, F. H. da Jornada, T. Cao and K. M. Dani, **Experimental measurement of the intrinsic excitonic wave function**, *Science Adv.* **7**, eabg0192 (2021)
- [19] A. Kunin, S. Chernov, J. Bakalis, Z. Li, S. Cheng, Z. H. Withers, M. G. White, G. Schönhense, X. Du, R. K. Kawakami and T. K. Allison, **Momentum-Resolved Intervalley and Intravalley Exciton Coupling in Monolayer WS₂**, *Phys. Rev. Lett.* **130**, 046202 (2023); doi: 10.1103/PhysRevLett.130.046202
- [20] O. Karni, I. Esin and K. M. Dani, **Through the lens of a momentum microscope: Viewing light-induced quantum phenomena in two-dimensional materials**, *Advanced Materials*, (2022); doi:10.1002/adma.202204120
- [21] D. Schmitt, J. P. Bange, W. Bennecke, A.A. AlMutairi, G. Meneghini, K. Watanabe, T. Taniguchi, D. Steil, D. R. Luke, R. T. Weitz, S. Steil, G. S. M. Jansen, S. Brem, E. Malic, S. Hofmann, M. Reutzler and S. Mathias, **Formation of Moiré interlayer excitons in space and time**, *Nature* **608**, 499 (2022); doi:10.1038/s41586-022-04977-7
- [22] O. Karni, E. Barré, V. Pareek, J. D. Georganas, M. K. L. Man, C. Sahoo, D. R. Bacon, X. Zhu, H. B. Ribeiro, A. L. O’Beirne, J. Hu, A. Al-Mahboob, M. M. M. Abdelrasoul, N. S. Chan, A. Karmakar, A. J. Winchester, B. Kim, K. Watanabe, T. Taniguchi, K. Barmak, J. Madéo, F. H. da Jornada, T. F. Heinz and K. M. Dani, **Moiré-localized interlayer exciton wavefunctions captured by imaging its electron and hole**, *Nature* **603**, 247 (2022); doi: 10.1038/s41586-021-04360-y
- [23] R. Wallauer, M. Raths, K. Stallberg, L. Münster, D. Brandstetter, X. Yang, J. Gütde, P. Puschnig, S. Soubatch, C. Kumpf, F. C. Bocquet, F. S. Tautz and U. Höfer, **Tracing orbital images on ultrafast time scales**, *Science* **371**, 1056 (2021); doi: 10.1126/science.abf3286
- [24] K. Baumgärtner, M. Reuner, C. Metzger, D. Kutnyakhov, M. Heber, F. Pressacco, C. H. Min, T. R. F. Peixoto, M. Reiser, C. Kim, W. Lu, R. Shayduk, W. M. Izquierdo, G. Brenner, F. Roth, A. Schöll, S. Molodtsov, W. Wurth, F. Reinert, A. Madsen, D. Popova-Gorelova, and M. Scholz, **Ultrafast orbital tomography of a pentacene film using time-resolved momentum microscopy at a FEL**, *Nat. Commun.*, **13**, 2741 (2022); doi: 10.1038/s41467-022-30404-6
- [25] A. Neef, S. Beaulieu, S. Hammer, S. Dong, J. Maklar, T. Pincelli, R. P. Xian, M. Wolf, L. Rettig, J. Pflaum and R. Ernstorfer, **Orbital-resolved observation of singlet fission**, *Nature* **616**, 275–279 (2023); doi: 10.1038/s41586-023-05814-1
- [26] J. Maklar, R. Stühler, M. Dendzik, T. Pincelli, S. Dong, S. Beaulieu, A. Neef, G. Li, M. Wolf, R. Ernstorfer, R. Claessen and L. Rettig, **Ultrafast Momentum-Resolved Hot Electron Dynamics in the Two-Dimensional Topological Insulator Bismuthene**, *Nano Lett.* **22**, 13, 5420 (2022); doi:10.1021/acs.nanolett.2c01462

- [27] S. Beaulieu, J. Schusser, S. Dong, M. Schüler, T. Pincelli, M. Dendzik, J. Maklar, A. Neef, H. Ebert, K. Hricovini, M. Wolf, J. Braun, L. Rettig, J. Minár and R. Ernstorfer, **Revealing Hidden Orbital Pseudospin Texture with Time-Reversal Dichroism in Photo-electron Angular Distributions**, Phys. Rev. Lett. **125**, 216404 (2020); doi:10.1103/PhysRevLett.125.216404
- [28] M. Schüler, T. Pincelli, S. Dong, T. P. Devereaux, M. Wolf, L. Rettig, R. Ernstorfer and S. Beaulieu, **Polarization-Modulated Angle-Resolved Photoemission Spectroscopy: Toward Circular Dichroism without Circular Photons and Bloch Wave-function Reconstruction**, Phys. Rev. X **12**, 011019 (2022)
- [29] M. Schüler and S. Beaulieu, **Probing topological Floquet states in WSe₂ using circular dichroism in time- and angle-resolved photoemission spectroscopy**, Comms. Phys. **5**, 164 (2022); doi:10.1038/s42005-022-00944-w
- [30] F. Pressacco, D. Sangalli, V. Uhlír, D. Kutnyakhov, J. Ander Arregi, S. Y. Agustsson, G. Brenner, H. Redlin, M. Heber, D. Vasilyev, J. Demsar, G. Schönhense, M. Gatti, A. Marini, W. Wurth and F. Sirotti, **Subpicosecond metamagnetic phase transition in FeRh driven by non-equilibrium electron dynamics**, Nat. Commun. **12**, 5088 (2021); doi: 10.1038/s41467-021-25347-3
- [31] V. Shokeen, M. Heber, D. Kutnyakhov, X. Wang, A. Yaroslavtsev, P. Maldonado, M. Berritta, N. Wind, L. Wenthaus, F. Pressacco, C.-H. Min, M. Nissen, S. K. Mahatha, S. Dziarzhytski, P.M. Oppeneer, K. Rossnagel, H.-J. Elmers, G. Schönhense and H. A. Dürr, **Real-time observation of phonon-electron energy flow in laser-heated Nickel**, Science Advances, in press (2024)
- [32] H. J. Elmers, S. V. Chernov, S. W. Dsouza, S. P. Bommanaboyena, S. Yu. Bodnar, K. Medjanik, S. Babenkov, O. Fedchenko, D. Vasilyev, S. Y. Agustsson, C. Schlueter, A. Gloskovskii, Yu. Matveyev, V. N. Strocov, Y. Skourski, L. Smejkal, J. Sinova, J. Minar, M. Kläui, G. Schönhense and M. Jourdan, **Néel vector induced manipulation of valence states in the collinear antiferromagnet Mn₂Au**, ACS Nano **14**, 17554 (2020); doi: 10.1021/acsnano.0c08215
- [33] O. Fedchenko, J. Minár, A. Akashdeep, S.W. D'Souza, D. Vasilyev, O. Tkach, L. Odenbreit, Q.L. Nguyen, D. Kutnyakhov, N. Wind, L. Wenthaus, M. Scholz, K. Rossnagel, M. Hoesch, M. Aeschlimann, B. Stadtmüller, M. Kläui, G. Schönhense, G. Jakob, T. Jungwirth, L. Smejkal, J. Sinova and H. J. Elmers, **Observation of time-reversal symmetry breaking in the band structure of altermagnetic RuO₂**, Science Advances, in press (2024); e-print on arXiv: 2306.02170
- [34] M. Lehr, B. Foerster, M. Schmitt, K. Krüger, C. Sönnichsen, G. Schönhense and H.-J. Elmers, **Momentum distribution of electrons emitted from resonantly excited individual gold nanorods**, Nano Letters **17**, 6606-6612 (2017); doi: 10.1021/acs.nanolett.7b02434
- [35] G. Schönhense and H.-J. Elmers, **Spin- and time-resolved photoelectron spectroscopy and diffraction studies using time-of-flight momentum microscopes**, J. Vac. Sci. Techn. A **40**, 020802 (2022), doi: 10.1116/6.0001500
- [36] O. Fedchenko, A. Winkelmann and G. Schönhense, **Structure Analysis using Time-of-Flight Momentum Microscopy with Hard X-rays: Status and Prospects**, J. Phys. Soc. Jpn. **91**, 091006 (2022), special volume "Hyper-Ordered Structures", doi:10.7566/JPSJ.91.091006
- [37] G.H. Fecher, O. Schmidt, Y. Hwu, G. Schönhense, **Multiphoton Photoemission Electron Microscopy Using Femtosecond Laser Radiation**, J. Electron Spectr. Relat. Phenom. **126** (2002) 77-87
- [38] M. Cinchetti, A. Gloskovskii, S. A. Nepjiko, G. Schönhense, H. Rochholz and M. Kreiter, **Photoemission Electron Microscopy as a tool for the investigation of optical near fields**, Phys. Rev. Lett. **95**, 047601 (2005)
- [39] F. Schertz, M. Schmelzeisen, R. Mohammadi, M. Kreiter, H.-J. Elmers and G. Schönhense, **Near Field of Strongly Coupled Plasmons: Uncovering Dark Modes**, Nano Letters **12**, 1885–1890 (2012)
- [40] B. Schönhense, K. Medjanik, O. Fedchenko, S. Chernov, M. Ellguth, D. Vasilyev, A. Oelsner, J. Viehhaus, D. Kutnyakhov, W. Wurth, H. J. Elmers and G. Schönhense, **Multidimensional Photoemission Spectroscopy – the Space-Charge Limit**, New J. of Physics **20**, 033004 (2018) doi: 10.1088/1367-2630/aaa262

- [41] G. Schönhense and B. Schönhense, **Reduction of space-charge interaction in electron-spectroscopic instruments**, German Patent, DE 10 2017 126 882.0 (filed Nov. 2017).
- [42] G. Schönhense, D. Kutnyakhov, F. Pressacco, M. Heber, N. Wind, S. Y. Agustsson, S. Babenkov, D. Vasilyev, O. Fedchenko, S. Chernov, L. Rettig, B. Schönhense, L. Wenthaus, G. Brenner, S. Dziarzhyski, S. Palutke, S. K. Mahatha, N. Schirmel, H. Redlin, B. Manschwetus, I. Hartl, Yu. Matveyev, A. Gloskovskii, C. Schlueter, V. Shokeen, H. Duerr, T. K. Allison, M. Beye, K. Rossnagel, H. J. Elmers and K. Medjanik, **Suppression of the vacuum space-charge effect in fs-photoemission by a retarding electrostatic front lens**, Rev. Sci. Instrum. **92**, 053703 (2021); doi: 10.1063/5.0046567
- [43] O. Tkach, S. Chernov, S. Babenkov, Y. Lytvynenko, O. Fedchenko, A. Hloskovskii, C. Schlueter, K. Medjanik, D. Vasilyev, H.-J. Elmers and G. Schönhense, **Asymmetric Electrostatic Dodecapole: Compact Bandpass Filter for Hard-X-ray Momentum Microscopy**, in preparation; e-print on arXiv:2303.18100v1 (2023)
- [44] P. A. Schultz, R. M. Van Ginhoven and A. H. Edwards, **Theoretical study of intrinsic defects in cubic silicon carbide 3C-SiC**, Phys. Rev. B **103**, 195202 (2021); doi:10.1103/PhysRevB.103.195202
- [45] Z. Guguchia, F. von Rohr, Z. Shermadini, A. T. Lee, S. Banerjee, A. R. Wieteska, C. A. Marianetti, B. A. Frandsen, H. Luetkens, Z. Gong, S. C. Cheung, C. Baines, A. Shengelaya, G. Taniashvili, A. N. Pasupathy, E. Morenzoni, S. J. L. Billinge, A. Amato, R. J. Cava, R. Khasanov and Y. J. Uemura, **Signatures of the topological $s +$ superconducting order parameter in the type-II Weyl semimetal T_d - MoTe_2** , Nature Commun. **8**, 1082 (2017); doi:10.1038/s41467-017-01066-6
- [46] O. Fedchenko, F. K. Diekmann, P. Russmann, M. Kallmayer, L. Odenbreit, S. M. Souliou, M. Frchet, A. Winkelmann, M. Merz, S. V. Chernov, D. Vasilyev, D. Kutnyakhov, O. Tkach, Y. Lytvynenko, K. Medjanik, C. Schlueter, A. Gloskovskii, T. R. F. Peixoto, M. Hoesch, M. Le Tacon, Y. Mokrousov, K. Rossnagel, G. Schönhense, H.-J. Elmers, **Doping-Induced Electronic and Structural Phase Transition in the Bulk Weyl Semimetal $\text{Mo}_{1-x}\text{W}_x\text{Te}_2$** , submitted, e-print on arXiv:2310.10593 (2023).
- [47] O. Fedchenko, A. Winkelmann, K. Medjanik, S. Babenkov, D. Vasilyev, S. Chernov, C. Schlueter, A. Gloskovskii, Yu. Matveyev, W. Drube, B. Schönhense, H. J. Elmers and G. Schönhense, **High-resolution hard-X-ray Photoelectron Diffraction in a Momentum Microscope - the Model Case of Graphite**, New J. of Phys. **21**, 113031 (2019), doi: 10.1088/1367-2630/ab51fe
- [48] K. Medjanik, S. V. Babenkov, S. Chernov, D. Vasilyev, B. Schönhense, C. Schlueter, A. Gloskovskii, Yu. Matveyev, W. Drube, H. J. Elmers and G. Schönhense, **Progress in HAXPES Performance Combining Full-Field k -Imaging with Time-of-Flight Recording**, J. of Synchr. Radiation **26**, 1996–2012 (2019), doi: 10.1107/S1600577519012773
- [49] Q. Nguyen, O. Tkach, O. Fedchenko, S. Chernov, N. Sirica, A. Mannix, Z. Zhang, L. Hoang, D. Kutnyakhov, F. Pressacco, J. Dilling, L. Bruckmeier, M. Scholz, F. Scholz, C. Schlueter, K. Rossnagel, M. Hoesch, R. Schoenlein, H.-J. Elmers and G. Schönhense, **Spectral-imaging of 2D magnetic semiconductor $V\text{-WS}_2$ using ToF-XPEEM**, in preparation
- [50] G. Schönhense and H. Spiecker, **Correction of Chromatic and Spherical Aberrations in Electron Microscopy Utilizing the Time-Structure of Pulsed Excitation Sources**, J. Vac. Sci. Technol. **B 20** (2002) 2526-2534
- [51] M. Patt, C. Wiemann, N. Weber, M. Escher, A. Gloskovskii, W. Drube, M. Merkel and C. M. Schneider, **Bulk sensitive hard x-ray photoemission electron microscopy**, Rev. Sci. Instrum. **85**, 113704 (2014); doi:10.1063/1.4902141
- [52] A. Bostwick, R.J. Koch and E. Rotenberg, see <https://sites.google.com/a/lbl.gov/maestro/instrumentation/nanoarpes>
- [53] S. Y. Agustsson, S. V. Chernov, K. Medjanik, S. Babenkov, O. Fedchenko, D. Vasilyev, C. Schlueter, A. Hloskovskii, Yu. Matveyev, K. Kliemt, C. Krellner, J. Demsar, G. Schönhense and H.-J. Elmers, **Temperature-dependent Change of the Electronic Structure in the Kondo Lattice System YbRh_2Si_2** , J. Phys. Condens. Matter **33**, 205601 (2021); doi: 10.1088/1361-648X/abe479

- [54] C. Xu, N. Barden, E. M. Alexeev, X. Wang, R. Long, A. R. Cadore, I. Paradisanos, A. K. Ott, G. Soavi, S. Tongay, G. Cerullo, A. C. Ferrari, O. V. Prezhdo and Z.-H. Loh, ***Ultrafast Charge Transfer and Recombination Dynamics in Monolayer–Multilayer WSe₂ Junctions Revealed by Time-Resolved Photoemission Electron Microscopy***, ACS Nano (2024); doi:10.1021/acsnano.3c06473
- [55] R. Gort, K. Bühlmann, S. Däster, G. Salvatella, N. Hartmann, Y. Zemp, S. Holenstein, C. Stieger, A. Fognini, T. U. Michlmayr, T. Bähler, A. Vaterlaus and Y. Acremann, ***Early Stages of Ultrafast Spin Dynamics in a 3d Ferromagnet***, Phys. Rev. Lett. **121**, 087206 (2018)
- [56] O. Fedchenko, L. Smejkal, M. Kallmayer, Ya. Lytvynenko, K. Medjanik, S. Babenkov, D. Vasilyev, M. Kläui, J. Demsar, G. Schönhense, M. Jourdan, J. Sinova and H.-J. Elmers, ***Direct Observation of Antiferromagnetic Parity Violation in the Electronic Structure of Mn₂Au***, J. Phys. Condensed Matter **34**, 425501 (2022); doi:10.1088/1361-648X/ac87e6